

To appear in the Astron. J. (July 2004)

Eclipse mapping of the flickering sources in the dwarf nova V2051 Ophiuchi ¹

Raymundo Baptista and Alexandre Bortoletto

Departamento de Física, UFSC, Campus Trindade, 88040-900, Florianópolis, Brazil

bap@astro.ufsc.br, alex@astro.ufsc.br

ABSTRACT

We report on the eclipse mapping analysis of an ensemble of light curves of the dwarf nova V2051 Oph with the aim to study the spatial distribution of its steady-light and flickering sources. The data are combined to derive the orbital dependency of the steady-light and the flickering components at two different brightness levels, named the 'faint' and 'bright' states. The differences in brightness are caused by long-term variations in the mass transfer rate from the secondary star. The white dwarf is hardly affected by the long-term changes. Its flux increases by only 10 per cent from the faint to the bright state, whereas the disk flux raises by a factor of 2. Eclipse maps of the steady-light show asymmetric brightness distributions with enhanced emission along the ballistic stream trajectory, in a clear evidence of gas stream overflow. The comparison between the steady-light maps of the faint and bright states suggests that the quiescent disk responds to changes in mass transfer rate in an homologous way. The ability to separate the orbital dependency of the low- and high-frequency flickering components allowed us to identify the existence of two different and independent sources of flickering in V2051 Oph. The low-frequency flickering arises mainly in the overflowing gas stream and is associated to the mass transfer process. Its maximum emission occurs at the position of closest approach of the gas stream to the white dwarf, and its spatial distribution changes in response to variations in the mass transfer rate. High-frequency flickering originates in the accretion disk, showing a radial distribution similar to that of the steady-light maps and no evidence of emission from the hot spot, gas stream or white dwarf. This disk flickering component has a relative amplitude of about 3 per cent of the steady disk light, independent of disk radius and brightness state. If the disk flickering is caused by fluctuations in the energy dissipation rate induced by magneto-hydrodynamic turbulence, its relative amplitude lead to a viscosity parameter $\alpha_{cool} \simeq 0.1 - 0.2$ at all radii for the quiescent disk. This value seems uncomfortably high to be accommodated by the disk instability model.

Subject headings: accretion, accretion disks – binaries: close – novae, cataclysmic variables – stars: dwarf novae – stars: oscillations – stars: individual (V2051 Ophiuchi)

1. Introduction

One of the long standing unsolved problems in accretion physics is related to the cause of flickering. The term is used to name the intrinsic, random brightness fluctuations of 0.01–1 magnitudes on timescales from seconds to dozens of minutes that are seen in the light curves of T Tauri stars (e.g., Herbst & Shevchenko 1999), mass-exchanging binaries (e.g., Augusteijn et al. 1992; Baptista, Bortoletto & Harlaftis 2002; Sokoloski, Bildsten & Ho 2001; Bruch 2000 and references therein) and AGNs (e.g., Garcia et al. 1999). Flickering is considered a basic signature of accretion (Warner 1995). Although the study of flickering (a time dependent phenomenon) may yield crucial information to the understanding of the viscosity in accretion disks, flickering is still the least studied and one of the most poorly understood of the accretion phenomena.

A promising step towards a better understanding of flickering consists in using indirect imaging techniques such as eclipse mapping (Horne 1985; Baptista 2001) to probe the surface distribution of the flickering sources in Cataclysmic Variables (CVs) [e.g., Welsh & Wood 1995]. In these close binaries mass is fed to a white dwarf (the primary) by a Roche lobe filling companion star (the secondary) via an accretion disk (for weakly magnetized white dwarfs) or column (for magnetic white dwarfs). A hot spot is expected to form where the gas stream from the donor star hits the outer edge of the accretion disk.

In a mass-exchanging binary, the orbital dependency of the flickering amplitude can be obtained by measuring the random brightness variations caused by flickering in an ensemble of light curves (i.e., the scatter curve) as a function of the orbital phase. Two different approaches exist for this purpose.

In its original form, the ‘ensemble’ method defines the scatter curve as the root-mean-square (rms) deviations of the set of light curves with respect to the mean orbital light curve (Horne & Stiening 1985). This definition yields good estimates of the flickering amplitude when the gross features of the light curve are stable in time and all the variability is caused by flickering. In the presence of long term brightness variations (i.e., changes on scales longer than the orbital period), the rms curve overestimates the flickering amplitude because the scatter produced by flickering is mixed with that caused by the long term brightness changes (e.g., Welsh & Wood 1995). A critical investigation of this problem is presented in Bruch (2000). Bennie, Hilditch & Horne (1996) devised a way to disentangle the scatter induced by long term variations from that caused by flickering. They associated a ‘reference’ out-of-eclipse flux level to each light curve in the data set. For a given phase bin, a plot of the flux of the data points versus the reference flux shows that these quantities are correlated. The slope of the correlation measures the long term change in the flux at that phase (a unity slope means that the flux at that phase varies in an 1:1 proportion with the reference flux) whereas the rms with respect to the best linear fit gives an unbiased measurement of the flickering component.

¹Based on observations made at Laboratório Nacional de Astrofísica/CNPq, Brazil.

In the ‘single’ method one quantifies the flickering in a set of light curves by measuring the scatter of each individual light curve with respect to a smoothed version of the light curve, and by combining the results from all light curves to derive a mean scatter curve (Bruch 1996). This is equivalent of a data filtering process, yielding the high-frequency components of the flickering. An intrinsic limitation of this method is the difficulty in separating the high-frequency flickering from rapid brightness changes, p.ex., caused by the eclipse, which may lead to the introduction of artifacts around sharp mid-ingress and mid-egress eclipse phases. A careful choice of the smoothing filter cut-off frequency is needed in order to avoid this problem.

The two techniques are complementary. The ‘ensemble’ method samples flickering at all frequencies. But because the power spectrum density of the flickering can be reasonably well described by a power-law $P(f) \propto f^{-\alpha}$, with $\alpha \simeq 1-3$ (Bruch 1992), an ensemble curve will normally be dominated by the low-frequency flickering components. On the other hand, the ‘single’ method produces curves which sample only the high-frequency flickering, with the cut-off frequency being defined by the smoothing filter width. Thus, the combination of both methods opens the possibility not only to probe the location of the flickering sources but also to separate low- and high-frequency components of the flickering. This may be very useful in the case where different flickering mechanisms lead to variability with distinct frequencies (e.g., see section 4).

V2051 Ophiuchi is a dwarf nova, a sub-class of CVs comprised by low-mass transfer binaries showing recurrent outbursts (caused by a sudden increase in the mass inflow in the disk) in which the brightness increases by factor of 5–100 on timescales of weeks to months (Warner 1995). V2051 Oph is distinguished among other ultra-short period eclipsing dwarf nova (i.e., Z Cha, OY Car and HT Cas) by its remarkable flickering activity (amplitude of $\gtrsim 30$ per cent), which is responsible for a variety of eclipse morphologies and usually masks the orbital hump associated to anisotropic emission from the hot spot (e.g., Warner & Cropper 1983; Cook & Brunt 1983). Based on their light curves, Warner & Cropper (1983) concluded that the flickering in V2051 Oph arises mainly from the inner disk regions, with only a minor contribution from the hot spot. Baptista et al. (1998a) caught the star in an exceptionally low brightness state during 1996 in which the flickering activity was mostly suppressed. They benefited from the clean view of the eclipses of the white dwarf and the faint hot spot at that epoch to derive basic parameters of the binary (e.g., masses, radii, orbital inclination).

Bruch (2000) applied the ‘single’ method to a large set of light curves of V2051 Oph to find that the flickering curve shows an eclipse ‘coincident with the white dwarf eclipse and definitely narrower than the disk eclipse’ as well as an orbital hump indicative that the bright spot contributes to the flickering in this star. However, the phase resolution of his scatter curve, $\Delta\phi = 0.01$ cycles, is not enough to adequately resolve the shape of the eclipse.

In this paper we present flickering curves of V2051 Oph of high phase resolution ($\Delta\phi = 0.002$ cycles) obtained with the ‘ensemble’ and ‘single’ methods, and we apply eclipse mapping techniques to these curves to map the flickering sources in this binary. The observations are

described in section 2. The data analysis is reported in section 3. The results are presented in section 4 and discussed in section 5. A summary of the conclusions is presented in section 6.

2. Observations

Time-series of high-speed CCD photometry of V2051 Oph in the B-band were obtained with an EEV camera (385×578 pixels, 0.58 arcsec pixel $^{-1}$) attached to the 1.6 m telescope of Laboratório Nacional de Astrofísica, in southern Brazil, from 1998 to 2002. The CCD camera is operated in a frame-transfer mode, with a negligible dead-time between exposures. It has a GPS board which sets its internal clock to UTC time to an accuracy better than 10 ms.

The observations are summarized in Table 1. The fourth column shows the time resolution of the observations in seconds (Δt), the fifth column lists the eclipse cycle number (E) and the last column gives an estimate of the quality of the observations. The seeing ranged from $1.0''$ to $2.2''$. The data comprise 36 eclipse light curves and only includes runs while V2051 Oph was in quiescence. The star went in outburst on 2000 July 31 and on 2002 August 6. These observations are not included here and will be presented in a separate paper.

All light curves were obtained with the same instrumental set and telescope, which ensures a high degree of uniformity to the data set.

Data reduction procedures included bias subtraction, flat-field correction, cosmic rays removal and aperture photometry extraction. Time-series were constructed by computing the magnitude difference between the variable and a reference comparison star with scripts based on the aperture photometry routines of the APPHOT/IRAF package². Light curves of other comparison stars in the field were also computed in order to check the quality of the night and the internal consistency and stability of the photometry over the time span of the observations.

The magnitude and colors of the reference star were tied to the Johnsons-Cousins UBVRI systems (Bessell 1990) from observations of this star and of blue spectro-photometric standard stars (Stone & Baldwin 1983) and standard stars of Graham (1982) made on 4 photometric nights. We used the relations of Lamla (1981) to transform UBVRI magnitudes to flux units. The B-band flux of the reference star was then used to transform the light curves of the variable from magnitude difference to absolute flux. We estimate that the absolute photometric accuracy of these observations is about 10 per cent. On the other hand, the analysis of the relative flux of the comparison stars of all observations indicates that the internal error of the photometry is less than 2 per cent. The error in the photometry of the variable is derived from the photon count noise and is transformed to flux units using the same relation applied to the data. The individual light curves have typical signal-to-noise ratios of $S/N = 40\text{--}50$ out-of-eclipse and of $S/N = 10\text{--}20$ at mid-eclipse.

²IRAF is distributed by National Optical Astronomy Observatories, which is operated by the Association of Universities for Research in Astronomy, Inc., under contract with the National Science Foundation.

The light curves were phase-folded according to the linear ephemeris (Baptista et al. 2003),

$$T_{mid} = BJDD \ 2443245.97752 + 0.0624278634 \times E. \quad (1)$$

Small phase corrections of -0.0018 (1998), -0.0012 (1999), $+0.0000$ (2000), $+0.0010$ (2001) and $+0.0061$ (2002) cycles were further applied to the data to make the center of the white dwarf eclipse coincident with phase zero. These corrections correspond to the measured O–C mid-eclipse time residual of the average eclipse light curve of each season with respect to the above ephemeris (see Baptista et al. 2003).

The individual light curves of V2051 Oph are shown superimposed in phase in Fig. 1. The upper panel depicts light curves of a comparison star of similar brightness. The constancy of its flux level over the time span of the observations attests that all variations seen in the lower panel are intrinsic to the variable. V2051 Oph was brighter in 1999 and 2000 by $\simeq 70$ per cent. Hereafter we will refer to the 1999+2000 data as to the ‘bright state’ and to the 1998+2001+2002 data as to the ‘faint state’. Thus, the data set of the faint and bright states comprise 20 and 16 light curves, respectively. We note that the data of a given observing season (3–5 days long) consistently belongs to a same brightness state. Hence, the brightness changes under consideration here occur on timescales longer than at least a few days. The comparison of the eclipse shape of both groups of light curves shows that the main difference is an increase in the brightness of the hot spot in the bright state in comparison with the faint state, indicating that significant long-term changes in the mass transfer rate from the secondary star occur on time scales of $\lesssim 1$ yr.

The scatter around the mean flux in V2051 Oph is perceptibly larger than that of the comparison star of similar brightness and is caused by flickering. The scatter is larger close to orbital hump maximum (suggesting that the bright spot contributes to the flickering) and is smaller during eclipse (indicating that the flickering sources are occulted at these phases). This is in line with the results of Bruch (2000). Remarkably, the scatter of the light curves of the bright state is larger than that of the faint state, suggesting a dependency of flickering amplitude with brightness level. This prompted us to perform separate analysis for the data of the two brightness states.

3. Data analysis

3.1. Light curve construction

Scatter curves for the faint and bright states were obtained with the ‘ensemble’ and ‘single’ methods as follows.

In order to compute the ‘single’ scatter curve we smoothed each light curve of a given brightness state with a median filter of length 170 s followed by a narrow box car filter (running average) of length 30 s, and subtracted the smoothed curve from the original data. The amount of filtering applied to the light curves is defined by two opposite requirements: (i) we wish to preserve the

lowest possible flickering frequency in the light curve after subtraction of the smoothed curve, but (ii) we need to avoid the artifacts that appear in the scatter curve around the sharp ingress/egress features of the white dwarf if too much filtering is applied. Smaller filter lengths produce noisy, low amplitude scatter curves because only the highest frequency components remain in the scatter curve after the subtraction of the smoothed curve. On the other hand, larger filter lengths introduce artificial ‘spikes’ in the resulting curve because the smoothed curve is no longer able to follow the sharp brightness changes that occur at white dwarf ingress and egress phases (e.g., see Fig.3 of Bruch 2000). The curves of the residuals from all individual light curves were combined and divided into a set of phases bins, ϕ . The mean scatter curve $\sigma_{tot}(\phi)$ was then computed from,

$$\sigma_{tot}^2(\phi) = \frac{1}{N(\phi) - 1} \sum_{i=1}^{N(\phi)} (f_i - \bar{f}_i)^2 , \quad (2)$$

where f_i and \bar{f}_i are, respectively, the flux of the i th data point in the original light curve and the corresponding flux in the smoothed curve, and $N(\phi)$ is the number of data points in each phase bin.

To compute the ‘ensemble’ scatter curve we defined a reference out-of-eclipse flux, f_{ref} (the mean flux over all the light curve excluding the primary eclipse and the orbital hump in the phase range -0.3 to $+0.15$ cycles) for each individual light curve. The ensemble of light curves of a given brightness state is then separated into a set of phase bins, ϕ . A linear fit to the $f_i \times f_{ref}(i)$ diagram of each phase bin yields an average flux (the flux of the fitted function at the median reference flux), an angular coefficient (which represents the secular variability at that phase), and a standard deviation with respect to the linear fit, σ_{tot} . By repeating the procedure for all phase bins we obtain the median orbital light curve (hereafter referred as the steady-light curve), the curve of the secular changes and the scatter curve, σ_{tot} ,

$$\sigma_{tot}^2(\phi) = \frac{1}{N(\phi) - 1} \sum_{i=1}^{N(\phi)} \{f_i - \bar{f}[f_{ref}(i)]\}^2 , \quad (3)$$

where $\bar{f}[f_{ref}(i)]$ is the value of the fitted linear function at the reference flux of the i th data point. The angular coefficient is sensitive to the range of values of the reference flux and to the scatter (i.e., the amount of flickering) at a given phase. Small Δf_{ref} and large scatter contribute to increase the uncertainty in the angular coefficient. This is particularly true for the faint state, for which the range of f_{ref} values is quite narrow. In order to improve the determination of the angular coefficient we increased the range of f_{ref} values by combining the data sets of both brightness states and we computed a single linear fit at each phase bin. Therefore, the curve of the secular changes is the same for both states but the scatter curve is computed separately for each brightness state.

Fig. 2 shows the $f_i \times f_{ref}(i)$ diagrams of the faint and bright states at three selected phases. A linear fit provides a good description of the relation between f_i and $f_{ref}(i)$ at all phases. The scatter around the linear fit is different for each data set and is generally larger for the bright state. As discussed in section 1, we note that using the rms with respect to the mean flux to compute the

scatter of a given data set overestimates the flickering contribution because no account is made of the linear trend in the observed fluxes caused by the long term changes.

The ‘single’ and ‘ensemble’ scatter curves have major contributions from the photon count statistics (Poisson noise, which is largely dominant in comparison to the sky scintillation) and from the intrinsic flickering activity. The flickering contribution at phase ϕ can then be obtained from the relation,

$$\sigma_f(\phi) = \sqrt{\sigma_{tot}^2(\phi) - \sigma_p^2(\phi)} \quad , \quad (4)$$

where

$$\sigma_p(\phi) = \frac{1}{N(\phi)} \sum_{i=1}^{N(\phi)} r_i \quad , \quad (5)$$

r_i is the Poisson noise (converted to flux units) of the i th data point, and $\sigma_{tot}^2(\phi)$ is obtained from Eqs.(2) and (3), respectively for the ‘single’ and ‘ensemble’ curves. In both cases, we adopt $\sigma_f(\phi) = 0$ when $\sigma_p(\phi) \geq \sigma_{tot}(\phi)$.

The error in the flickering curve $S_{\sigma_f}(\phi)$ is derived by error propagation including the error in the standard deviation σ_{tot} (e.g., Lupton 1993),

$$S_{\sigma_f}(\phi) = \frac{1}{\sigma_f(\phi)} \sqrt{\frac{\sigma_{tot}^4(\phi)}{2(N(\phi) - 1)} + \sigma_p^2(\phi) \text{Var}[\sigma_p(\phi)]} \quad (6)$$

where

$$\text{Var}[\sigma_p(\phi)] = \left(\frac{1}{N(\phi)} \sum_{i=1}^{N(\phi)} r_i^2 \right) - \left(\frac{1}{N(\phi)} \sum_{i=1}^{N(\phi)} r_i \right)^2 \quad . \quad (7)$$

The value of $S_{\sigma_f}(\phi)$ is meaningless when $\sigma_f(\phi) = 0$.

The steady-light curves, the curves of the secular change, and the ‘ensemble’ and ‘single’ flickering curves for the faint and bright states are shown in Fig. 3.

In order to check the consistency of our results, we repeated the procedure including different subsets of the light curves in the analysis with the ‘ensemble’ and ‘single’ methods of each brightness state. As expected, the uncertainties in the flickering curves increase by reducing the number of curves in the subset. However, the results are not sensitive to the particular subset of light curves included in the analysis (provided that at least 8-10 light curves are included in each subset) and are the same under the uncertainties. The computed curves will be discussed in detail in section 4.1.

3.2. Eclipse mapping

The steady-light, secular changes, and flickering curves were analyzed with eclipse mapping techniques (Baptista & Steiner 1993) to solve for a map of the disk surface brightness distribution and for the flux of an additional uneclipsed component in each case. The uneclipsed component

accounts for all light that is not contained in the eclipse map (i.e., light from the secondary star and/or a vertically extended disk wind). The reader is referred to Rutten, van Paradijs & Tinbergen (1992) and Baptista, Steiner & Horne (1996) for a detailed description of and tests with the uneclipsed component.

Our eclipse map is a flat cartesian grid of 101×101 pixels centered on the primary star with side $2 R_{L1}$ (where R_{L1} is the distance from the disk center to the inner Lagrangian point). We adopt $R_{L1} = 0.422 R_{\odot}$ (Baptista et al. 1998a). The eclipse geometry is defined by the mass ratio q and the inclination i . We adopted the parameters of Baptista et al. (1998a), $q = 0.19$ and $i = 83^\circ$, which corresponds to an eclipse phase width of $\Delta\phi = 0.0662$. This combination of parameters ensures that the white dwarf is at the center of the map.

In the standard eclipse mapping method all variations in the light curve are interpreted as being caused by the changing occultation of the emitting region by the secondary star. Thus, out-of-eclipse brightness changes (e.g., orbital modulation due to anisotropic emission from the bright spot) have to be removed before the light curves can be analyzed. This is done by fitting a spline function to the phases outside eclipse, dividing the light curve by the fitted spline, and scaling the result to the spline function value at phase zero. This procedure removes orbital modulations with only minor effects on the eclipse shape itself.

For the reconstructions we adopted the default of limited azimuthal smearing of Rutten et al. (1992), which is better suited for recovering asymmetric structures than the original default of full azimuthal smearing (cf. Baptista, Steiner & Horne 1996). The reader is referred to Baptista, Harlaftis & Steeghs (2000) and Baptista (2001) for eclipse mapping simulations which evaluate the ability of the eclipse mapping method to reconstruct asymmetric structures in eclipse maps.

The statistical uncertainties of the eclipse maps are estimated with a Monte Carlo procedure (e.g., Rutten et al. 1992). For a given input data curve a set of 20 artificial curves is generated, in which the data points are independently and randomly varied according to a Gaussian distribution with standard deviation equal to the uncertainty at that point. The artificial curves are fitted with the eclipse mapping algorithm to produce a set of randomized eclipse maps. These are combined to produce an average map and a map of the residuals with respect to the average, which yields the statistical uncertainty at each pixel. The uncertainties obtained with this procedure are used to estimate the errors in the derived radial temperature and intensity distributions.

4. Results

4.1. Morphology of the light curves

The large amplitude flickering usually seen in V2051 Oph makes it hard to distinguish the white dwarf and the hot spot eclipses in individual light curves. By averaging many individual light curves we were able of reducing the influence of flickering in the steady-light curves, leading

to a clean view of the eclipse shape.

The steady-light curves (Fig. 3a) show the broad eclipse of a faint quiescent disk and the sharp ingress and egress of the white dwarf and hot spot eclipses – which occur at orbital phases in agreement with the photometric model of Baptista et al. (1998a). The flux of the hot spot is larger at ingress than at egress, demonstrating that it is the source of the orbital hump. We modeled the out of eclipse flux of the steady-light curves as the sum of a half-sinusoidal function (i.e., the amplitude of the sine term is forced to be zero for $\pi < \phi < 2\pi$) and a constant flux level in order to measure the relative amplitude and phase of maximum of the orbital hump. The steady-light curve of the faint state shows a weak orbital hump (with an amplitude of 12 per cent of the total flux) centered at phase $\phi_{max} = -0.16 \pm 0.02$ cycles. We estimate a hot spot contribution of $f_{hs}(\text{faint}) = 0.35 \pm 0.05$ mJy from its ingress feature. The orbital hump is more pronounced in the bright state, with a relative amplitude of 20 per cent and maximum at phase $\phi_{max} = -0.13 \pm 0.02$ cycles. The hot spot flux at ingress in this case is $f_{hs}(\text{bright}) = 0.65 \pm 0.05$ mJy.

The measured hot spot flux at ingress is larger than the predicted flux of the orbital hump at the same phase. This is an indication that the hot spot has an additional isotropic component. We subtracted the predicted flux of the orbital hump at hot spot ingress from the measured hot spot flux at ingress to find isotropic components of 0.25 ± 0.06 mJy and 0.27 ± 0.06 mJy, respectively for the faint and bright states. Thus, the anisotropic component of the hot spot emission increases by a factor of 3 from the faint to the bright state, whereas the isotropic component remains essentially at the same flux level.

The curve of the secular changes (Fig. 3b) shows a pronounced orbital hump and a V-shaped eclipse with ingress coincident with hot spot ingress and minimum displaced towards positive phases, indicating a significant contribution from the hot spot and gas stream to the long-term brightness variations. Remarkably, there is no clear sign of the sharp white dwarf ingress/egress features in the eclipse, revealing that the white dwarf gives negligible contribution to the long-term brightness changes. The shape of the curve of the secular changes is identical to that of the curve of the difference between the bright and faint states under the uncertainties. The latter can be obtained by scaling the former by a factor of 1/3. This is a direct consequence of the ‘ensemble’ assumption that the flux at a given phase scales linearly with the overall brightness level,

$$f(\phi, x) = f_0(\phi) + x \cdot \left(\frac{\partial f}{\partial f_{ref}} \right)_{\phi} . \quad (8)$$

The difference between any two brightness levels $\Delta f = f_2 - f_1$ is obtained by multiplying the secular change $(\partial f / \partial f_{ref})_{\phi}$ by a scaling factor x independent of phase. In fact, the light curve of the faint and bright states themselves can be recovered by adding appropriate proportions x of the curve of the secular changes to a common baseline light curve f_0 .

The ‘ensemble’ curves (Fig. 3c) are distinct from the corresponding steady-light curves. The eclipse is narrower and displaced towards positive phases. There is no perceptible reduction in flux at the ingress phase of the white dwarf, although there is a sharp recovery coincident with

the white dwarf egress in the curve of the bright state. This suggests that this star is not an important contributor to the low-frequency flickering, at least in the faint state. The orbital hump is relatively more prominent than in the steady-light curves (relative amplitudes of 70 and 40 per cent, respectively for the faint and bright states), indicating a significant (anisotropic) contribution of the hot spot to the low-frequency flickering. The absolute amplitude of the hump is larger in the bright state than in the faint state, but the relative amplitude is smaller. This indicates that the contribution of the hot spot to the low-frequency flickering is diluted by other sources in the bright state. The differences in out-of-eclipse level between the two ‘ensemble’ curves reflect the larger amplitude of the flickering in the bright state. Together with the difference in eclipse shape, this justifies the choice to perform separate flickering analysis for each brightness state.

The lower amplitude of the ‘single’ curves (Fig. 3d) in comparison with the ‘ensemble’ curves is in agreement with the expectation that the ‘single’ procedure extracts only the low-amplitude, high frequency flickering components of the light curve. The eclipse shapes and the gross features of the ‘single’ curves are remarkably different from those of the ‘ensemble’ curves. The orbital hump is weaker in the faint state (relative amplitude of 30 per cent) and almost nonexistent in the bright state (amplitude of less than 10 per cent). This suggests that the hot spot contributes little to the high-frequency flickering. The eclipses are centered at phase zero but are shallow and wider than the eclipse of the white dwarf, indicating that the high-frequency flickering is not localized in the vicinities of the white dwarf but arises from a larger region.

Our qualitative analysis reveal that flickering of different frequencies in V2051 Oph arise from different regions and possibly have different origins.

4.2. The contribution of the white dwarf

We separated the contribution of the white dwarf from the steady-light curves with a light curve decomposition technique (Wood, Irwin & Pringle 1985) in order to compute eclipse maps only of the quiescent disk.

Figure 4 illustrates the procedure with the steady-light curve of the bright state. The contact phases of the white dwarf can be identified as rapid changes in the slope of the light curve (Fig. 4a). The original light curve is smoothed with a median filter (3 data points) and its numerical derivative is calculated. The derivative curve is smoothed with the same median filter as above to reduce noise and improve the detection of the white dwarf features. The ingress/egress of the white dwarf are seen as those intervals where the derivative of the light curve is significantly different from zero (Fig. 4b). A spline function is fitted to the remaining regions in the derivative to remove the contribution from the extended and slowly varying eclipse of the disk. Estimates of the white dwarf flux are obtained by integrating the spline-subtracted derivative at ingress and egress. The light curve of the white dwarf is then reconstructed by assuming that its flux is zero between ingress and egress and that it is constant outside eclipse (Fig. 4c). The separated light curve of the accretion

disk (plus hot spot) is obtained by subtracting the reconstructed white dwarf light curve from the original light curve (Fig. 4d). The eclipse maps of the steady-light shown in section 4.4 were computed using the white dwarf subtracted steady-light curves.

The derived B-band fluxes of the white dwarf in the steady-light curves of the faint and bright states are, respectively, 0.45 ± 0.02 mJy and 0.51 ± 0.02 mJy. We applied the same procedure to the B-band light curve of Baptista et al. (1998a) to find a flux of 0.9 ± 0.1 mJy. The B-band average out-of-eclipse flux at that epoch was 1.4 ± 0.1 mJy, while the average out-of-eclipse level of the steady-light curves of the faint and bright states are, respectively, 1.44 ± 0.03 mJy and 2.52 ± 0.06 mJy. Hence, the white dwarf flux in our data is lower by a factor of 2 than that of the 'low' brightness state of 1996 – where accretion has probably reduced to a minimum and the bare white dwarf could be seen thru a residual, optically thin disk (Baptista et al. 1998a).

Because accretion is expected to increase the surface temperature of the white dwarf (Godon & Sion 2003 and references therein), it is hard to explain the reduction in flux in terms of a lower white dwarf temperature during the epoch of our observations (where accretion was certainly taking place) in comparison with the 'low' state of 1996 (where only residual accretion may have occurred). On the other hand, the discrepancy is plausibly explained if the inner disk regions were optically thick at the epoch of our observations and veiled the lower white dwarf hemisphere from view, thereby leading to a reduction in white dwarf flux by the observed factor. This is in agreement with the results of Vrielmann, Stiening & Offutt (2002) which found that the accretion disk of V2051 Oph in quiescence consists of an optically thin, low density chromospheric layer (responsible for the emission lines) on top of a denser and cooler opaque disk gas.

Since we have the white dwarf flux at only one wavelength it is not possible to simultaneously fit its temperature and solid angle. Therefore, we adopted $R_{wd} = 0.0103 R_{\odot}$ (Baptista et al. 1998a) and a distance of 146 pc (Vrielmann et al. 2002), and assumed a fixed white dwarf solid angle of $\theta^2 = 7.82 \times 10^{-3} [R_{wd}/0.0103 R_{\odot}]^2 [d/0.146 Kpc]^{-2} (R_{\odot}/Kpc)^2$ for our observations and twice that value for the observations of Baptista et al. (1998a). We fitted the observed flux densities from synthetic photometry with white dwarf atmosphere models (Gänsicke, Beuermann & de Martino 1995) to find $T_{wd} = (24.2 \pm 0.6) \times 10^3$ K and $(25.8 \pm 0.5) \times 10^3$ K, respectively for the faint and bright states. The inferred temperature for the 'low' brightness state of Baptista et al. (1998a) is the same as that for the faint state, since the measured white dwarf flux and the solid angle are scaled by exactly the same factor.

The derived temperatures are significantly larger than the previous estimates of $\simeq 15000$ K (Catalán et al. 1998; Steeghs et al. 2001) and 19600 K (Vrielmann et al. 2002). This seems contradictory because V2051 Oph was 60 per cent brighter at the epoch of the observations of Vrielmann et al. (2002) in comparison with our observations, whereas the data of Catalán et al. (1998) correspond to the 'low' brightness state of Baptista et al. (1998a) and those of Steeghs et al. (2001) are contemporary with our 1998 observations. On the other hand, the inferred white dwarf temperatures can be made compatible with the values derived by those authors if the distance is

reduced to about 100 pc. Independent estimates of the distance to V2051 Oph would be helpful to clarify this point.

The difference in white dwarf temperature between the faint and bright states is small but significant at the 3σ level. It is possibly the result of extra accretional heating in consequence of the larger mass transfer rate of the bright state (e.g., Godon & Sion 2003).

4.3. The hot spot and the disk radius

An estimate of the disk radius can be obtained from the ingress and egress phases of the hot spot (ϕ_{hi} , ϕ_{he}) under the assumption that the hot spot is located where the stream of transferred matter hits the outer edge of the accretion disk. Measuring hot spot phases in V2051 Oph is not as straightforward as measuring white dwarf eclipse phases because the hot spot is less compact than the white dwarf (see Fig. 4). We can nevertheless use the derivative technique of section 4.2 to estimate the ingress/egress phases of its brightest part.

The measurements were made on average light curves of each observing season (which comprise time intervals of a few days) in order to minimize the blur in the ingress/egress phases caused by possible changes in disk radius with time. The results are consistent for the data of a given brightness state and are also similar for the faint and bright states. We find $\phi_{hi} = -0.017 \pm 0.002$, $\phi_{he} = +0.080 \pm 0.002$ for the faint state and $\phi_{hi} = -0.018 \pm 0.002$, $\phi_{he} = +0.082 \pm 0.003$ for the bright state. The circles that pass thru the points defined by these pairs of phases are $R_{hs} = 0.46 \pm 0.02 R_{L1}$ and $R_{hs} = 0.47 \pm 0.02 R_{L1}$, respectively for the faint and bright states. This is perceptibly smaller than the disk radius of $0.56 \pm 0.02 R_{L1}$ found by Baptista et al. (1998a) for the ‘low’ brightness state.

The radial position of the hot spot is similar in the faint and bright states, but its flux increased by a factor of about 2 from one brightness state to the other (Section 4.1). The luminosity of the hot spot is inversely proportional to its distance to the disk center and directly proportional to the rate at which mass is injected into the outer accretion disk. Thus, the only sensible way on changing the flux of a hot spot at a fixed radial position is by varying the mass injection rate (i.e., the mass transfer rate). In addition, inspection of the curve of the difference between the steady-light curves of the faint and bright states (Fig. 3a) confirms that the change in brightness level is mainly the consequence of enhanced emission from the hot spot and gas stream region in the bright state. This underscores the conclusion drawn in section 2 that the long term brightness changes are caused by variations in mass transfer rate.

4.4. Steady-light and flickering disk structures

The maps of the surface brightness of the steady-light, secular changes and flickering are shown in Fig. 5. Circles of radii $0.27 R_{L1}$ (the circularization radius for V2051 Oph, see Baptista et al. 1998a) and $0.47 R_{L1}$ (the disk radius for the bright state) are depicted in each eclipse map. Average radial intensity distributions for the eclipse maps in Fig. 5 are shown in Fig. 6. The circularization radius (R_{circ}) is indicated in the ‘ensemble’ panel. Dotted lines in the other panels depict the slope of a power-law radial intensity dependency $I(R) \propto R^\alpha$ in each case.

The asymmetric steady-light eclipse shapes, with minima displaced towards positive phases, lead to asymmetric brightness distributions with enhanced emission along the gas stream region. This brightness enhancement traces the ballistic stream trajectory. It goes well beyond the outer disk rim and can be clearly seen down to the region where the stream trajectory passes ‘behind’ the white dwarf (i.e., at the disk side farther away from the secondary star). This is a clear evidence of gas stream overflow in V2051 Oph.

The maximum emission along the stream does not lie on the hot spot location but at the position of closest approach to the white dwarf. This can be explained if the gas stream emission is caused by the progressive release of gravitational potential energy of the infalling gas (into heat and, thereafter, radiation), which has a maximum at the closest distance to the central source. An alternative interpretation is that the enhancement is caused by reprocessing of radiation from the inner disk regions on a vertically extended bulge along the gas stream trajectory. In this model, the increased brightness at the region of closest approach to the white dwarf could be the consequence of the larger solid angle of this region as seen from the illuminating source.

The hot spot and the gas stream region are more pronounced in the bright state map, in agreement with the inferred higher inflow of mass from the companion star in this brightness level. Aside from the difference in brightness level, the two eclipse maps are very similar. Both show a flat radial intensity distribution in the inner disk regions ($I \propto R^{-0.3}$) which decreases sharply for $R \gtrsim 0.23 R_{L1}$ (with a slope $I \propto R^{-2}$).

Not surprisingly, the map of the secular changes is very similar to the steady-light maps, with a flat brightness distribution in the inner regions and enhanced emission along the gas stream. In fact, its radial intensity distribution is hardly distinguishable from that of the steady-light map of the bright state. The similarities between the steady-light maps and the map of the secular changes indicates that the quiescent disk of V2051 Oph responds to changes in mass transfer rate in an homologous way (except for the gas stream region, which has a more pronounced increase in brightness than the rest of the disk).

The ‘ensemble’ flickering maps are noticeably different from the corresponding maps of the steady-light. The narrower eclipse shapes tell us that the center of the flickering brightness distributions are displaced towards the disk side farther away from the secondary star (for the eclipse to be shorter than the white dwarf eclipse), whereas the offset towards positive phases indicate that

the brightness distributions are skewed towards the trailing side of the disk (the one containing the gas stream trajectory). The ‘ensemble’ map of the faint state shows an arc-shaped structure running along the gas stream trajectory and extending for almost all azimuths at a radial position coincident with the circularization radius. There is no evidence of emission from the vicinities of the white dwarf (the decrease in flickering amplitude at disk center is statistically significant at the 10σ level, see ahead). The ‘ensemble’ map of the bright state similarly shows an arc-shaped structure along the gas stream trajectory, with the brightness enhancement starting at a larger radius in comparison with the faint state map. In contrast with the faint state map, the map of the bright state indicates a clear contribution from the disk center.

In analogy with the steady-light maps, the maximum of the flickering amplitude along the stream trajectory on both ‘ensemble’ maps does not occur at the location of the hot spot but around the position of closest approach to the white dwarf. Hence, the conclusion of Warner & Cropper (1983) that the flickering in V2051 Oph arises in general ‘in the inner disk region with only a minor contribution from the hot spot’ is consistent with our findings.

The ‘ensemble’ maps show that the low-frequency flickering in V2051 Oph is associated mostly to the hot spot and gas stream, with additional contribution from the innermost disk regions in the bright state.

The ‘single’ maps are remarkably different from the ‘ensemble’ maps, but bear resemblance with the steady-light maps. The broad and wide eclipse shapes of the ‘single’ curves map into extended, shallow and fairly axi-symmetric brightness distributions with no clear evidence of the hot spot, gas stream or white dwarf. In fact, the ‘single’ maps are slightly asymmetric in the sense that there is a dearth of emission along the gas stream trajectory – the high-frequency flickering amplitude is smaller at the regions where the low-frequency flickering is stronger. The ‘single’ radial brightness distributions (Fig. 6) are very similar to the radial distributions of the steady-light, without the asymmetries caused by the gas stream emission. As with the steady-light, the amplitude of the high-frequency flickering also increases in an homologous way with the mass transfer rate. This indicates that the high-frequency flickering is associated to the accretion disk.

We used Monte Carlo simulations (section 3.2) for an assessment of the statistical significance of the observed structures in the flickering maps. Each flickering map was divided by the map of the residuals with respect to the mean map to produce a map of the inverse of the relative errors, or a signal-to-noise ratio map (e.g., Harlaftis et al. 2004). The S/N maps are overplotted on the corresponding flickering maps as contour lines for $S/N=10$ and 15 in Fig. 7. It can be seen that the statistical significance of the structures in all flickering maps is larger than the 10σ level. The ‘ensemble’ curves have higher S/N and result in maps with a typical significance at the 20σ level.

Fig. 8 shows the relative amplitude of the low- and high-frequency flickering as a function of radius. These curves are obtained by dividing the radial intensity distribution of each flickering map by that of the steady-light map of the corresponding brightness state. The large scatter with respect to the mean amplitude in the ‘ensemble’ case for radii $0.2 < R/R_{L1} < 0.5$ is caused by the

strong asymmetries in the corresponding flickering maps.

The ‘single’ flickering shows a relative amplitude of about 3 per cent, independent of disk radius and brightness state. The amplitude of the high-frequency flickering scales with the brightness of the quiescent steady-light disk, thereby confirming the previous conclusion that this flickering component is intimately associated to the physics of the accretion disk itself. This lends support to models which attempt to explain flickering in terms of physical processes in the accretion disk, such as unsteady release of energy at the disk surface because of convective, turbulent vertical motions (Geertsema & Achterberg 1992; Bruch 1992) or events of magnetic reconnection in the disk chromosphere (Kawaguchi et al. 2000). These models predict a power-law behaviour for the power spectrum of this disk flickering, with a rise of power towards lower frequencies (e.g., Geertsema & Achterberg 1992).

On the other hand, the relative amplitude of the ‘ensemble’ flickering varies significantly with radius and brightness level. Its maximum occurs in a range of radii around the circularization radius. The relative amplitude is consistently larger than that of the high-frequency flickering and reaches 26 per cent at $R = R_{circ}$ in the faint state. The maximum of the distribution moves to a larger radius in the bright state, probably in response to the increased mass transfer rate. The clear association between the low-frequency flickering and the hot spot/gas stream and its sensitivity to the mass transfer rate indicates that its origin is connected to the mass transfer process. Possible explanations include unsteady (or clumpy) mass transfer from the secondary star (Warner & Nather 1971) and turbulence generated by the progressive impact of the overflowing gas stream with the disk (Shu 1976).

The uneclipsed component of each curve is shown as a horizontal dashed line in the left panels of Fig. 5. It is negligible in all cases, except for the ‘ensemble’ curve of the bright state. In this case we find an uneclipsed flux of 0.017 ± 0.006 mJy, corresponding to 8 per cent of the total flux. This may indicate the development of a vertically-extended clumpy or turbulent wind from the inner disk regions in response to the increase in mass transfer rate. The bright stripe running from the disk center towards the ‘back’ side of the disk (i.e., the disk hemisphere farther away from the secondary star) in the corresponding ‘ensemble’ map may be the projection onto the orbital plane of the base of this disk wind. If this is correct, the geometry of this structure suggests that the disk wind is highly collimated. Support in favor of this scenario comes from the work of Warner & O’Donoghue (1987), who found evidence of an additional asymmetric, variable source of light outside of the orbital plane in V2051 Oph. Alternatively, it may be that part of the incoming unsteady stream of gas is flung out of the binary towards the L2 point (to the left of the eclipse maps in Fig. 5) in analogy to the ‘magnetic propeller’ scenario of Horne (1999), in which infalling blobs of plasma are accelerated by the magnetic field of a spinning white dwarf. The recent discovery of a coherent 52 s oscillation in V2051 Oph (Steeghs et al. 2001) suggests that this system may indeed harbor a magnetic, spinning white dwarf.

4.5. The flickering power density spectrum

So far we have concentrated on the analysis of the data in the time domain. Here, we investigate the dependency of the flickering in V2051 Oph with frequency and we use the results to check the consistency of our previous separation of the flickering into low- ('ensemble') and high- ('single') frequency components.

The average steady-light curve of the corresponding brightness state was subtracted from each individual light curve to remove the DC component and a Lomb-Scargle periodogram (Press et al. 1992) was calculated. The periodograms of all light curves of a given brightness state were combined to yield a mean periodogram and a standard deviation with respect to the mean. Fig. 9 shows the average power density spectrum (PDS) of the faint and bright states binned to a resolution of 0.02 units in $\log(\text{frequency})$. The dotted lines indicate the $1-\sigma$ limits on the average power in each case. The PDS show a flat distribution at low frequencies and are well described at high frequencies by power-laws $P(f) \propto f^\alpha$ with $\alpha = -1.2$ and -1.7 , respectively for the faint and bright states. The frequency below which each distribution becomes flat is $f_c(\text{faint}) = 7 \times 10^{-4}$ Hz ($t_c = 23.8$ min) and $f_c(\text{bright}) = 2 \times 10^{-3}$ Hz ($t_c = 8.3$ min). The slopes of the PDS distributions are consistent with those seen in other CVs, which can be well described at high frequencies by power laws with an average exponent of $\alpha = -2.0 \pm 0.8$ (Bruch 1992).

The results of section 4.4 lead us to associate the disk-related flickering to the power-law PDS region and the stream-related flickering to the flat PDS region. The low-frequency cut-off of the filter applied in the 'single' procedure is indicated in Fig. 9. The cut-off frequency is such that the resulting 'single' curves frame only the power-law region of the PDS (the disk flickering), whereas the 'ensemble' curves are dominated by the higher power of the regions in which the distribution is flat (the stream flickering).

We also computed Lomb-Scargle periodograms of the residual curves used to derive the 'single' scatter curves (section 3.1). These periodograms were combined to produce average 'single' PDS of the faint and bright states. As expected, the 'single' PDS show a significant reduction of power at frequencies lower than the smoothing filter cut-off frequency of the 'single' procedure. The total, integrated power of the 'single' PDS corresponds to 30-40 per cent of the integrated power of the corresponding, unfiltered PDS shown in Fig. 9, in good agreement with the flux ratio between the 'single' and 'ensemble' flickering curves.

4.6. Radial brightness temperature distributions

A simple way of testing theoretical disk models is to convert the intensities in the steady-light eclipse maps to blackbody brightness temperatures, which can then be compared to the radial run of the effective temperature predicted by steady state, optically thick disk models. As pointed out by Baptista et al. (1998b), a relation between the monochromatic brightness temperature and

the effective temperature is non-trivial, and can only be properly obtained by constructing self-consistent models of the vertical structure of the disk. Since we only have B-band light curves, a detailed disk spectrum modeling is beyond the reach with our data set. Thus, although the brightness temperature should be close to the effective temperature for the optically thick disk regions, the results from this section should be looked with caution.

The disk radial temperature distributions were derived from the steady-light maps without the contribution of the white dwarf. The blackbody brightness temperature that reproduces the observed surface brightness at each pixel was calculated assuming a distance of 146 pc to the system (Vrielmann et al. 2002). We neglected interstellar reddening since there is no sign of the interstellar absorption feature at 2200 Å in spectra obtained with the Hubble Space Telescope (Baptista et al. 1998a). The disk was then divided in radial bins of $0.05 R_{L1}$ and a median brightness temperature was derived for each bin. These are shown in Fig. 10 as interconnected symbols. The dashed lines show the $1-\sigma$ limits on the average temperatures. The larger σ values of the bright state distribution reflect the azimuthal asymmetries in the intermediate disk regions ($0.2 - 0.3 R_{L1}$) caused by the enhanced emission along the gas stream trajectory. Steady-state disk models for mass accretion rates of $\log \dot{M} = -9, -10$, and $-11 M_{\odot} \text{ yr}^{-1}$ are plotted as dotted lines for comparison.

The distributions are flatter than the $T \propto R^{-3/4}$ law for optically-thick steady-state disks for $R \lesssim 0.23 R_{L1}$. The temperatures in the faint state range from 8000 K in the inner disk ($R = 0.1 R_{L1}$) to about 4700 K in the outer disk regions ($R \simeq 0.5 R_{L1}$). The temperatures in the bright state are higher than those of the faint state by about 1000 K at all disk radii. The inferred mass accretion rates (in $M_{\odot} \text{ yr}^{-1}$) are $\log \dot{M}_{0.1} = (-11.0 \pm 0.2)$ at $R = 0.1 R_{L1}$ and $\log \dot{M}_{0.3} = (-10.05 \pm 0.05)$ at $R = 0.3 R_{L1}$ for the faint state, and $\log \dot{M}_{0.1} = (-10.8 \pm 0.2)$ and $\log \dot{M}_{0.3} = (-9.92 \pm 0.02)$ for the bright state. The derived disk temperatures and mass accretion rates are consistent with (although slightly smaller than) those inferred by Vrielmann et al. (2002). We note that the inferred brightness temperatures of the quiescent disk of V2051 Oph are systematically higher than those derived for the dwarf nova OY Car (Wood et al. 1989) and Z Cha (Wood et al. 1986) in quiescence. If the disk of V2051 Oph is optically thick, the large range of \dot{M} required by the brightness temperature distributions implies that gas is piling up in the outer disk regions during quiescence at a rate $\simeq 10$ times higher than that at which the gas in the inner disk falls onto the white dwarf.

If the distance is reduced to 100 pc, the disk brightness temperatures become lower by $\simeq 1000$ K in the inner disk regions and by $\simeq 500$ K in the outer disk. The inferred mass accretion rates will become 40 per cent smaller than the above values.

According to the disk instability model, dwarf novae outbursts are driven by a thermal instability within their disks (e.g., Lasota 2001 and references therein). In this model, there is a critical effective temperature, $T_{\text{eff}}(\text{crit})$, below which the disk gas should remain while in quiescence in

order to allow the thermal instability to set in (e.g., Warner 1995),

$$T_{\text{eff}}(\text{crit}) = 7432 \left(\frac{R}{R_{L1}} \right)^{-0.105} \left(\frac{M_1}{0.78 M_{\odot}} \right)^{-0.15} K. \quad (9)$$

This relation is plotted in Fig. 10 as a dot-dashed line. It can be seen that the inferred brightness temperatures of the quiescent disk of V2051 oph are everywhere below $T_{\text{eff}}(\text{crit})$, in agreement with the prediction of the disk instability model. The agreement is better if the distance is reduced to 100 pc.

5. Discussion

5.1. A comparison with previous results

The eclipse in the flickering ('single') curve of Bruch (2000) is narrower and deeper than that of our 'single' curves and led him to conclude that the flickering in V2051 Oph originates in the innermost disk regions. This is in contrast with our results. Here we explore a possible explanation for this difference.

Bruch's (2000) smoothing filter cut-off frequency of 0.018 Hz implies that only flickering occurring on time scales shorter than 1 minute are included in his 'single' curve, whereas our 'single' curves comprise flickering of time scales shorter than 2.8 min. Taking into account the power-law dependency of the flickering distribution, this means that his flickering curve samples typically higher frequencies than our 'single' curves. Both the disk turbulence and the magnetic reconnection flickering models predict a spatial segregation of flickering events, with higher frequency flickering occurring closer to disk center (Geertsema & Achterberg 1992; Kawaguchi et al. 2000). Thus, a 'single' flickering curve sampling higher frequencies should lead to a narrower and deeper eclipse than a curve sampling lower frequencies as the distribution of the flickering sources in the former case is more concentrated towards the disk center. This could explain the observed difference in shape of 'single' curves with different cut-off frequencies.

We tested this idea by creating 'single' curves using the same cut-off frequency of Bruch (2000). Although the resulting curves are too noisy to allow drawing any firm conclusion, we found marginal evidence that the increase in cut-off frequency indeed lead to a narrower and deeper eclipse shape. A larger data set (to increase the S/N ratio of the 'single' curves) is required in order to provide a more conclusive test of this prediction.

It is worth mentioning that V2051 Oph was perceptibly brighter at the epoch sampled by Bruch's (2000) data (out-of-eclipse magnitude of $B \simeq 15.0$ mag) than at the epoch of our observations ($B \simeq 15.7 - 16.2$ mag). We remark that if the flickering distribution (and the relative importance of each of the flickering sources) changes significantly with brightness level, the comparison made in this section may be misleading. In addition, we note that the flickering curve of Bruch (2000) was derived from a data set containing a mix of white light observations obtained

with photomultipliers of different effective wavelengths (e.g., the ‘blue’ Amperex 56DVP vs. the ‘red’ RCA 31034A) including both data in quiescence and in outburst (Warner & Cropper 1983; Warner & O’Donoghue 1987) and, therefore, should be looked with some caution.

5.2. Estimating the viscosity parameter α

Geertsema & Achterberg (1992) investigated the effects of magneto-hydrodynamic (MHD) turbulence in an accretion disk. They found that the rate of energy dissipated per unit area at the disk surface shows large fluctuations which could be a source of flickering in CVs and x-ray binaries. Here we use their model and the observed relative amplitude of the ‘single’ flickering to estimate the viscosity parameter α (Shakura & Sunyaev 1973) of the quiescent accretion disk in V2051 Oph.

In the model of Geertsema & Achterberg (1992), the rms value of the fluctuations $\sigma(D)$ in the average rate of energy dissipated per unit area $\langle D \rangle$ is given by,

$$\frac{\sigma(D)}{\langle D \rangle} \simeq \frac{2.5}{\sqrt{N}} , \quad (10)$$

where,

$$D(r) = \frac{3GM_1\dot{M}}{8\pi r^3} \left(1 - \sqrt{\frac{r_1}{r}}\right) , \quad (11)$$

M_1 and r_1 are, respectively, the mass and radius of the white dwarf, and N , the number of turbulent eddies that contribute to the local fluctuation, is given by,

$$N(r) = 4\pi \frac{r}{H} \left(\frac{H}{L}\right)^2 \simeq 1.25 \times 10^3 \left(\frac{H}{L}\right)^2 , \quad (12)$$

where H is the disk scale height, L is the size of the largest turbulent eddies, and we assumed $H/r \simeq 10^{-2}$, typical of thin disks (e.g., Frank, King & Raine 1992). The α -parameter of Shakura & Sunyaev (1973) can be written as,

$$\alpha \simeq 0.9 \left(\frac{L}{H}\right)^2 \simeq 1130 \frac{1}{N} \simeq 180 \left[\frac{\sigma(D)}{\langle D \rangle}\right]^2 . \quad (13)$$

If the disk flickering is caused by fluctuations in the energy dissipation rate induced by MHD turbulence, the relative amplitude of this flickering component is a direct measurement of the ratio $\sigma(D)/\langle D \rangle$. Replacing the observed relative amplitude of the ‘single’ flickering in the above expressions we find $N \simeq 7000$, $L/H \simeq 0.42 (10^2 H/r)^{-1/2}$, and a viscosity parameter $\alpha \simeq 0.16 (10^2 H/r)^{-1}$. Because the relative amplitude of the ‘single’ flickering is constant with radius, the inferred viscosity parameter is the same at all disk radii.

The inferred viscosity parameter is significantly higher than expected for a quiescent, cool disk in the disk instability model ($\alpha_{cool} \simeq 10^{-2}$). In fact, it is of the order of the expected viscosity of hot

disks during dwarf novae outbursts ($\alpha_{hot} \simeq 0.1 - 0.2$, see e.g., Lasota 2001). Thus, if our assumption that MHD turbulence is the cause of the disk flickering is correct, the estimated viscosity parameter is uncomfortably high to be accommodated by the disk instability model.

One way to avoid this inconsistency is if the accretion disk of V2051 Oph is geometrically thick ($H/r \gtrsim 0.05$). However, there is a problem with this thick disk scenario. It would require a disk half-opening angle of $\beta \gtrsim 3^\circ$. At the high inclination of V2051 Oph, this would lead to an apparent brightness contrast between the emission from the disk hemisphere closest to (the ‘front’ side) and farthest from (the ‘back’ side) the secondary star, with the ‘back’ side being a factor of at least 2.5 brighter than the ‘front’ side ³. There is no evidence of front-back brightness contrast in our steady-light eclipse maps.

An important implication of the derived high value of the viscosity parameter α is that the quiescent disc of V2051 Oph should be in a steady-state (because the resulting viscous timescale, $\simeq 30$ days, is short in comparison with the typical timescale between outbursts, $\simeq 10^3$ days). This is apparently in contradiction with the flat radial temperature profile derived in section 4.6. However, the optical spectrum of V2051 Oph is dominated by strong Balmer lines and a Balmer jump in emission, indicating important contribution from optically thin gas. In this case, the assumption that the B-band blackbody brightness temperature reflects the gas effective temperature probably fails and the comparison of the radial temperature distribution with theoretical disk models (Fig. 10) is possibly meaningless.

6. Summary

We applied the ‘single’ and ‘ensemble’ methods to a uniform set of light curves of V2051 Oph to derive the orbital dependency of its steady-light, long-term brightness changes, low- and high-frequency flickering components. The data can be grouped in two different brightness levels, named the ‘faint’ and ‘bright’ states. The differences in brightness level are caused by variations in mass transfer rate from the secondary star (by a factor of 2) occurring on time scales longer than a few days and shorter than 1 yr. The white dwarf is hardly affected by these long-term changes. Its flux increases by only 10 per cent from the faint to the bright state, whereas the disk flux raises by a factor of 2.

Eclipse maps of the steady-light show asymmetric brightness distributions with enhanced emission along the ballistic stream trajectory, in a clear evidence of gas stream overflow. The maximum emission along the stream occurs at the position of closest approach to the white dwarf. The hot spot and the gas stream region are more pronounced in the bright state map, in agreement with the inferred higher mass transfer rate of this brightness level. Aside of this, the eclipse maps of

³We note that this exercise does not take into account possible limb darkening effects, which would make the brightness ratio even larger than assumed.

the faint and bright states and of the secular changes are similar, showing a flat radial intensity distribution in the inner disk regions ($I \propto R^{-0.3}$) which decreases sharply for $R \gtrsim 0.23 R_{L1}$ (with a slope $I \propto R^{-2}$). These similarities lead us to conclude that the quiescent disk of V2051 Oph responds to changes in mass transfer rate in an homologous way.

Our flickering mapping analysis reveal the existence of two different sources of flickering in V2051 Oph, which lead to variability at distinct frequencies. The low-frequency flickering arises mainly in the overflowing gas stream and is connected to the mass transfer process. Its maximum emission occurs around the position at which the stream is closer to the white dwarf and the amplitude reaches 10 – 25 per cent of the steady-light intensity at the same location. In the bright state there is additional contribution from the disk center and an extra, uneclipsed component of 8 per cent of the total flux which may indicate the development of a vertically-extended clumpy or turbulent wind from the inner disk regions. Unsteady mass transfer or turbulence generated after the shock between the stream and the disk material may be responsible for this stream flickering component.

The high-frequency flickering is produced in the accretion disk. It is spread over the disk surface with a radial distribution similar to that of the steady-light maps and it shows no evidence of emission from the hot spot, gas stream or white dwarf. This disk flickering component has a relative amplitude of about 3 per cent of the steady-light, independent of disk radius and brightness state. If the disk flickering is caused by fluctuations in the energy dissipation rate induced by MHD turbulence, its relative amplitude lead to a viscosity parameter $\alpha \simeq 0.1 – 0.2$ at all radii for the quiescent disk of V2051 Oph. This value seems uncomfortably high to be accommodated by the disk instability model.

Previous studies suggested that flickering may originate from two separate sources, the hot spot and a turbulent inner disk region (Warner 1995; Bruch 2000). Our flickering mapping experiment reveals a more complex situation, in which flickering arising from the inner disk regions may in fact have the same origin as the hot spot flickering, namely, the mass transfer process. Stream flickering from the inner disk regions may be largely dominant over the disk flickering if gas stream overflow occurs in a quiescent dwarf novae, because the contribution from the disk flickering in this case is small (since the disk itself is relatively faint). Also, although the hot spot contributes to the flickering, it is a minor source in comparison to the inner gas stream in this situation. This seems to be the case in V2051 Oph. On the other hand, if the disk flickering amplitude is a fixed fraction of the steady disk light, it might become the dominant flickering source and may appear as arising mainly from the innermost disk regions in a high- \dot{M} , nova-like system as the surface brightness of the bright, opaque disks of these systems decreases sharply with radius.

Finally, we note that the measurement of the disk flickering component yields a novel and independent way to estimate the disk viscosity parameter α . The large value found in this first experiment seems to favor the mass-transfer instability model (Warner 1995 and references therein).

This work was partially supported by the PRONEX/Brazil program through the research grant FAURGS/CNPq 66.2088/1997-2. RB and AB acknowledge financial support from CNPq/Brazil, respectively through grants no. 300 354/96-7 and 577 266/1997-7.

REFERENCES

Augusteijn, T., et al. 1992, *A&A*, 265, 177

Baptista, R. 2001, in *Astrotomography: Indirect Imaging Methods in Observational Astronomy*, eds. H. M. J. Boffin, D. Steeghs & J. Cuypers (Berlin: Springer-Verlag), 307

Baptista, R. & Steiner, J. E. 1993, *A&A*, 277, 331

Baptista, R., Steiner, J. E. & Horne, K. 1996, *MNRAS*, 282, 99

Baptista, R., Catalán, M. S., Horne, K. & Zilli, D. 1998a, *MNRAS*, 300, 233

Baptista, R., Horne, K., Wade, R., Hubeny, I., Long, K. & Rutten, R. G. M. 1998b, *MNRAS*, 298, 1079

Baptista, R., Harlaftis, E. T. & Steeghs, D. 2000, *MNRAS*, 314, 727

Baptista, R., Bortoletto, A. & Harlaftis, E. T. 2002, *MNRAS*, 335, 665

Baptista, R., Borges, B. W., Bond, H. E., Jablonski, F., Steiner, J. E. & Grauer, A. D. 2003, *MNRAS*, 345, 889

Bennie, P. J., Hilditch, R. & Horne, K. 1996, in *Cataclysmic Variables and related objects*, IAU Coll. 158, eds. A. Evans & J. Wood (Dordrecht: Kluwer), 33

Bessell, M. A. 1990, *PASP*, 102, 1181

Bobinger, A., Horne, K., Mantel, K. H. & Wolf, S. 1997, *A&A*, 327, 1023

Bruch, A. 1992, *A&A*, 266, 237

Bruch, A. 1996, *A&A*, 312, 97

Bruch, A. 2000, *A&A*, 359, 998

Catalan, M. S., Horne, K., Cheng, F.-H., Marsh, T. R. & Hubeny I. 1998, in *Wild Stars in the Old West*, ASP Conf. Series 137, p. 426

Cook, M. C. & Brunt, C. C. 1983, *MNRAS*, 205, 465

Frank, J., King, A. R., & Raine, D. J. 1992, *Accretion Power in Astrophysics* - 2nd edition (Cambridge: Cambridge University Press)

Gänsicke, B. T., Beuermann, K. & de Martino, D. 1995, *A&A*, 303, 127

Garcia, A., Sodré, L., Jablonski, F. J. & Terlevich, R. J. 1999, *MNRAS*, 309, 803

Geertsema, G. T. & Achterberg, A. 1992, *A&A*, 255, 427

Godon, P. & Sion, E. M. 2003, *ApJ*, 586, 427

Graham, J. A. 1982, *PASP*, 94, 244

Harlaftis, E. T., Baptista, R., Morales-Rueda, L., Marsh, T. R. & Steeghs, D. 2004. *A&A*, 417, 1063

Horne, K. 1985, *MNRAS*, 213, 129

Horne, K. 1999, in *Magnetic Cataclysmic Variables*, ASP Conf. Series Vol. 157, eds. K. Mukai & C. Hellier (San Francisco: ASP), 349

Horne, K. & Stiening, R. F. 1985, *MNRAS*, 216, 933

Herbst, W. & Shevchenko, K. S. 1999, *AJ*, 118, 1043

Kawaguchi, T., Mineshige, S., Machida, M., Matsumoto, R. & Shibata K. 2000, *PASJ*, 52, L1

Lamla, E. 1981, in *Landolt-Börnstein - Numerical Data and Functional Relationships in Science and Technology*, Vol. 2, eds. K. Schaifers & H. H. Voigt (Berlin: Springer-Verlag)

Lasota, J.-P. 2001, *New Astron. Reviews*, 45, 449

Lupton, R. 1993, *Statistics in Theory and Practice*, (Princeton: Princeton University Press)

Press, W. H., Flannery, B. P., Teukolsky, S. A. & Vetterling, W. T. 1992, *Numerical Recipes in C* (Cambridge: Cambridge University Press)

Rutten, R. G. M., van Paradijs, J. & Tinbergen, J. 1992, *A&A*, 260, 213

Shakura, N. I. & Sunyaev, R. A. 1973, *A&A*, 24, 337

Shu, F. H. 1976, in *Structure and Evolution of Close Binary Systems*, IAU Symp. 73, eds. P. Eggleton, S. Mitton & J. Whelan (Dordrecht: Reidel), 253

Sokoloski, J. L., Bildsten, L. & Ho W. C. G. 2001, *MNRAS*, 326, 553

Stone, R. P. S. & Baldwin, J. A. 1983, *MNRAS*, 204, 347

Steeghs, D., O'Brien, K., Horne, K., Gomer, R. & Oke, J. B. 2001, *MNRAS*, 323, 484

Vrielmann, S., Stiening, R. F. & Offutt, W. 2002, *MNRAS*, 334, 608

Warner, B. 1995, *Cataclysmic Variable Stars* (Cambridge: Cambridge University Press)

Warner, B. & Nather, R. E. 1971, MNRAS, 152, 219

Warner, B. & Cropper, M. 1983, MNRAS, 203, 909

Warner, B. & O'Donoghue D. 1987, MNRAS, 224, 733

Welsh, W. F. & Wood, J. H. 1995, in Flares and Flashes, eds. J. Greiner, H. W. Duerbeck & Roald E. Gershberg (Berlin: Springer-Verlag), 300

Wood, J. H., Irwin, M. J. & Pringle, J. E. 1985, MNRAS, 214, 475

Wood, J. H., Horne, K., Berriman, G., Wade, R., O'Donoghue, D. & Warner, B. 1986, MNRAS, 219, 629

Wood, J. H., Horne, K., Berriman, G. & Wade, R. 1989, ApJ, 341, 974

Table 1. Journal of the observations

date	Start (UT)	Number of exposures	Δt (s)	E (cycle)	Phase range	brightness state	Quality ^a
1998 Jul 25	22:15	283	3	124535	+0.00, +0.31	faint	B
	23:15	888	5	124536	-0.32, +0.50	faint	B
1998 Jul 26	00:29	804	5	124537	-0.50, +0.27	faint	B
	21:40	828	5	124551	-0.37, +0.50	faint	A
	22:58	1077	5	124552	-0.37, +0.50	faint	A
1998 Jul 27	00:28	1079	5	124553	-0.37, +0.50	faint	A
	01:58	1077	5	124554	-0.37, +0.50	faint	A
	03:28	785	5	124555	-0.50, +0.39	faint	A
1999 Jul 12	22:42	1098	5	130174	-0.19, +0.83	bright	A
1999 Jul 13	03:02	669	5	130177	-0.28, +0.34	bright	A
1999 Jul 15	21:32	344	5	130221	+0.10, +0.47	bright	A
	22:11	548	5	130222	-0.47, +0.50	bright	B
	23:38	733	5	130223	-0.50, +0.50	bright	C
1999 Jul 16	01:08	114	5	130224	-0.50, -0.34	bright	C
2000 Jul 28	22:37	726	5	136293	-0.19, +0.50	bright	A
	23:39	941	5	136294	-0.50, +0.50	bright	A
2000 Jul 29	01:08	1074	5	136295	-0.50, +0.50	bright	A
	02:38	538	5	(136296)	-0.50, +0.23	bright	A
	21:23	281	5	136308	+0.01, +0.50	bright	A
	22:07	1079	5	136309	-0.50, +0.50	bright	A
	23:37	1078	5	136310	-0.50, +0.50	bright	A
2000 Jul 30	01:07	860	5	136311	-0.50, +0.30	bright	A
	02:43	848	5	136312	-0.43, +0.36	bright	A
	21:54	986	5	136325	-0.62, +0.29	bright	B
2001 Jun 25	22:34	587	5	141611	-0.05, +0.50	faint	A
	23:24	960	5	141612	-0.50, +0.50	faint	A
2001 Jun 26	00:53	614	5/10	141613	-0.50, +0.64	faint	A
	04:12	359	10	141615	-0.29, +0.38	faint	C
2001 Jun 27	21:38	539	10	141643	-0.64, +0.36	faint	B
	23:23	541	10	141644	-0.47, +0.53	faint	B
2001 Jun 28	01:20	520	10	141645	-0.16, +0.80	faint	B
	05:37	327	10	141648	-0.31, +0.29	faint	B
	23:09	393	15	141660	-0.60, +0.50	faint	C
2001 Jun 29	00:49	303	15	141661	-0.50, +0.34	faint	C
2002 Aug 04	22:28	626	10	148099	-0.66, +0.50	faint	B
2002 Aug 05	00:13	672	10	148100	-0.50, +0.75	faint	B

^aSky conditions: A= photometric (main comparison stable), B= good (some sky variations), C= poor (large variations and/or clouds)

Fig. 1.— Bottom: light curves of V2051 Oph in 1998, 2001 and 2002 (gray dots) and in 1999 and 2000 (solid symbols). Top: The light curves of a comparison star of similar brightness. Vertical dashed lines mark the ingress/egress phases of the white dwarf, whereas dotted lines indicate the ingress phase of the bright spot and the beginning/end of the eclipse of an accretion disk of radius $0.6 R_{L1}$. The scatter around the mean flux yields an indication of the flickering amplitude at each phase.

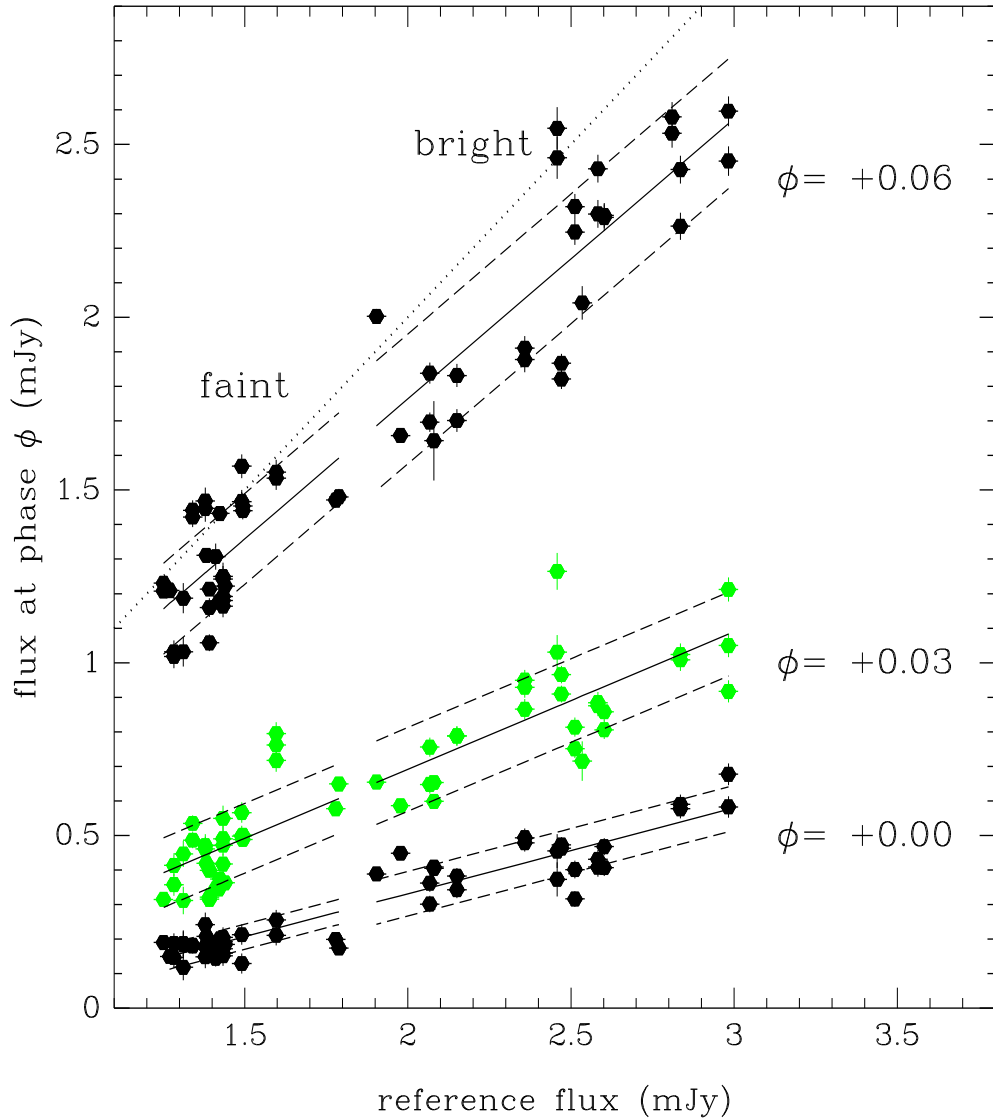


Fig. 2.— $f_i \times f_{ref}(i)$ diagrams at three selected orbital phases for the faint and bright states (filled symbols with error bars). Solid lines show the best linear fit to the data. Dashed lines indicate the standard deviation (flickering + photon count noise) with respect to the fit in each case. A dotted line indicates the unity slope.

Fig. 3.— (a) Median (steady-light) curves for the faint (left) and bright (right) states. The lower curve in the right panel is the difference between the two curves (in the sense bright minus faint). (b) The curve of the secular changes, repeated in the right panel for visualization purposes. (c) The ‘ensemble’ curves. The lower curve in each panel indicates the contribution of the Poisson noise, $\sigma_p(\phi)$, to the total scatter. (d) The ‘single’ curves; the contribution of the Poisson noise is the same as in (c). The ingress/egress phases of the white dwarf and bright spot are indicated, respectively, by dashed and dotted vertical lines. Representative error bars are shown in all panels.

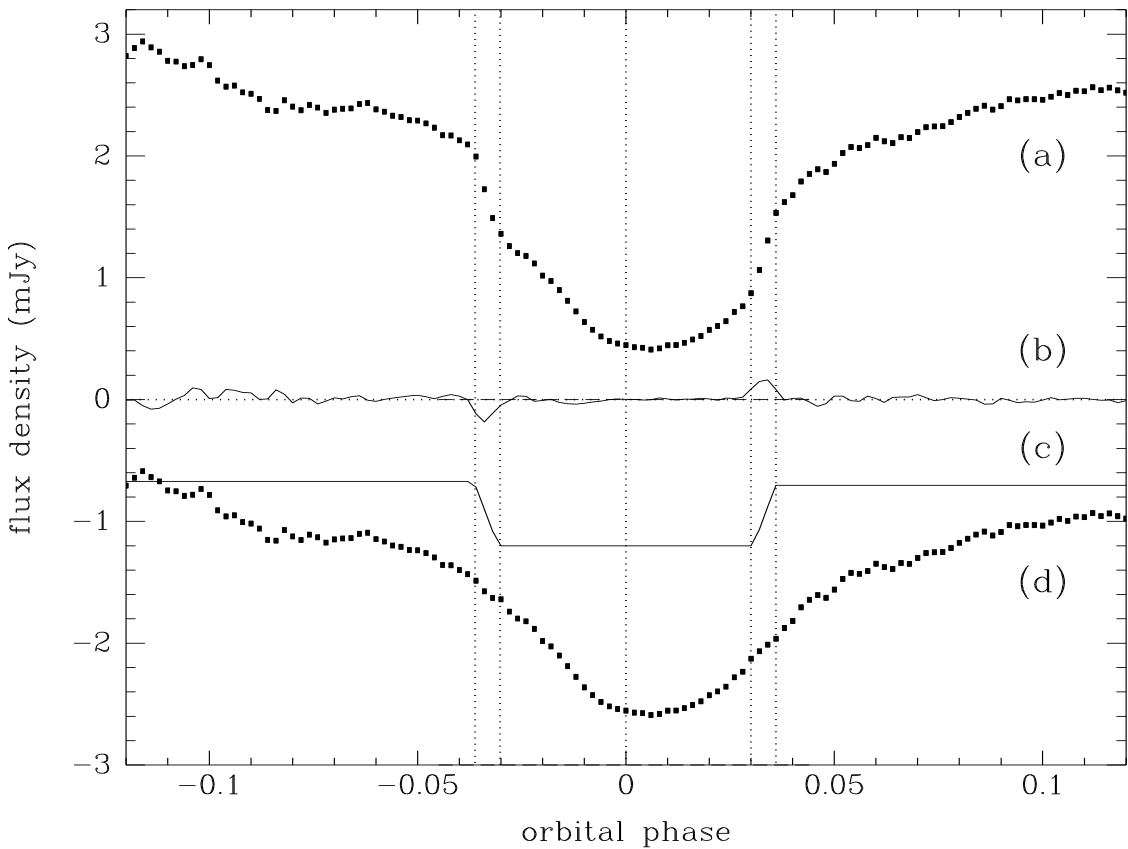


Fig. 4.— Removing the contribution of the white dwarf from the steady-light curve of the bright state. (a) the original light curve; (b) the median-filtered derivative of light curve (a) after removing the slowly-varying disk component; (c) the reconstructed white dwarf light curve, shifted downwards by 1.2 mJy; (d) the light curve without the white dwarf component, shifted downwards by 3 mJy. Vertical dotted lines mark the mid-eclipse and the contact phases of the white dwarf.

Fig. 5.— Left: the steady-light, secular changes and flickering curves (dots) and the corresponding eclipse mapping models (solid lines). Vertical dotted lines mark the ingress/egress phases of the white dwarf and mid-eclipse. The curves of the bright state were vertically displaced for visualization purposes. Horizontal dotted lines indicate the true zero level and horizontal dashed lines mark the uneclipsed component in each case. Right panels: the corresponding eclipse maps in a logarithmic greyscale. Dotted lines depict the primary Roche lobe, the gas stream trajectory, and circles of radius 0.27 and $0.47 R_{L1}$. The log of intensity scale of each case is indicated in the corresponding greyscale bar.

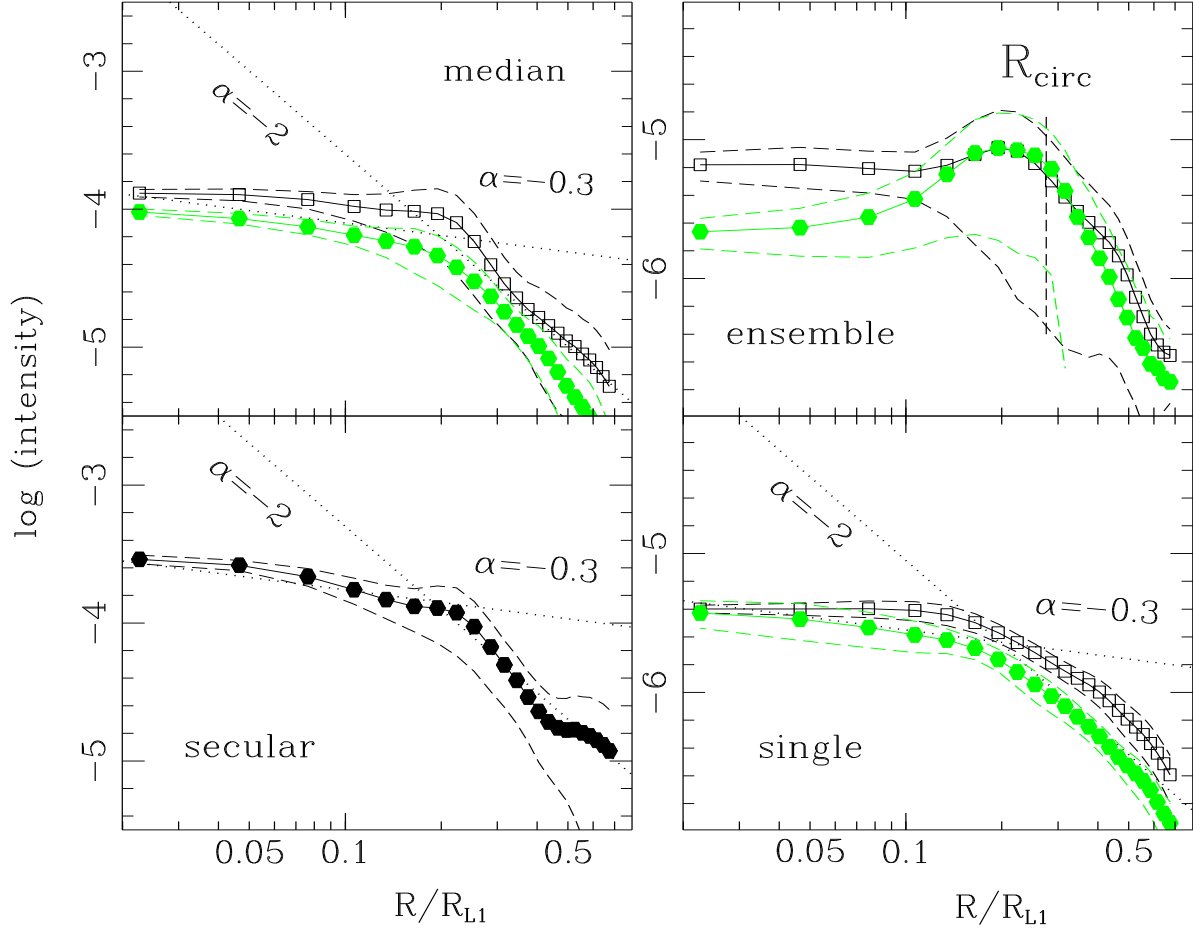


Fig. 6.— Radial intensity distribution of the steady-light (top left-hand panel), the secular changes (bottom left-hand panel), the ‘ensemble’ (top right-hand panel) and ‘single’ (bottom left-hand panel) eclipse maps. The distributions of the faint and bright states are indicated, respectively, by filled circles and open squares. Dashed lines show the 1- σ limit on the average intensity for a given radius. Abscissae are in units of the distance from disk center to the inner Lagrangian point R_{L1} . The circularization radius $R_{circ} = 0.27 R_{L1}$ (Baptista et al. 1998a) is indicated in the ‘ensemble’ panel. Dotted lines in the other panels depict the slope of a power-law radial intensity dependency $I(R) \propto R^\alpha$ in each case.

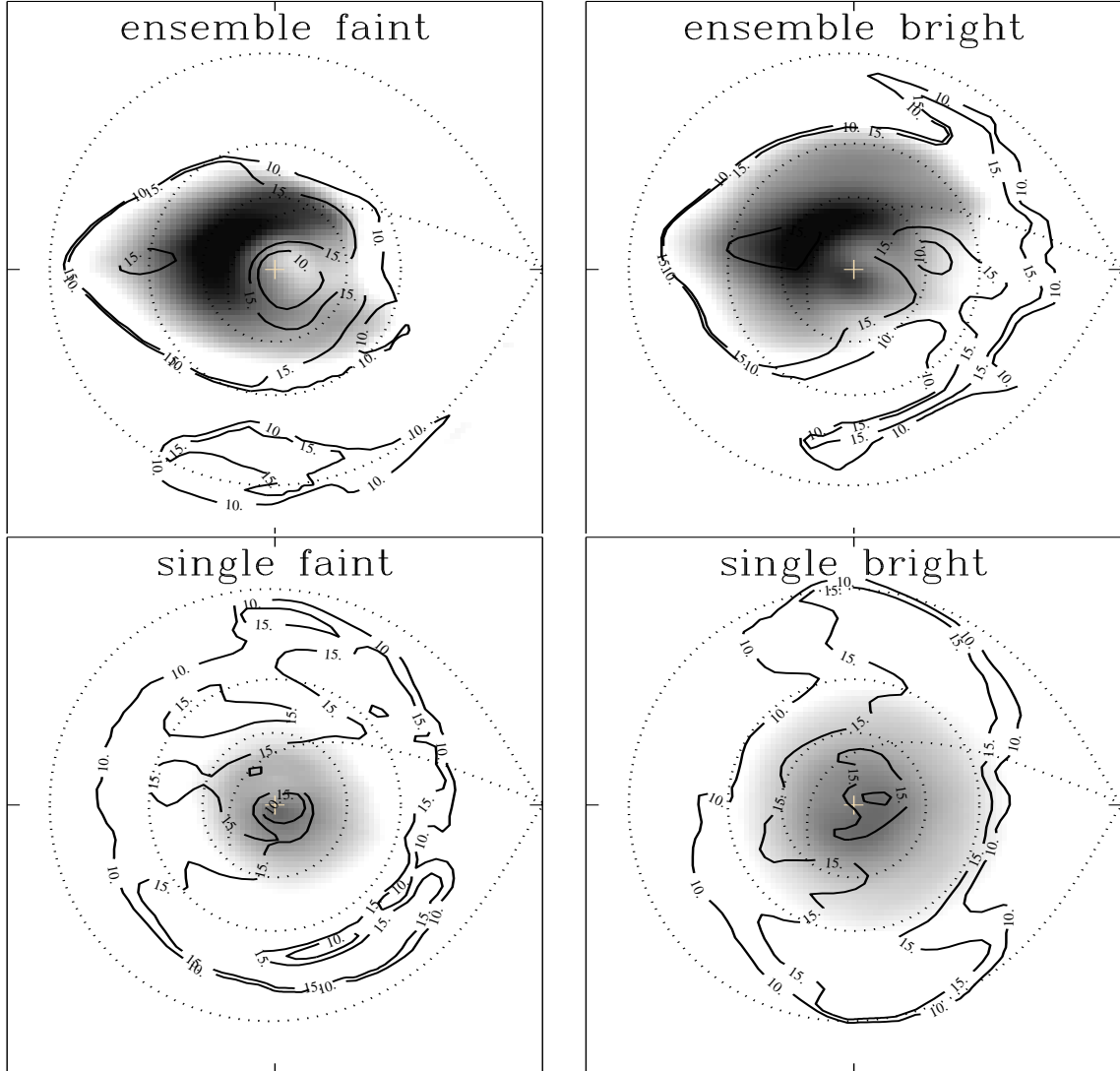


Fig. 7.— The statistical significance of the flickering maps. Contour lines for $S/N=10$ and 15 are overplotted on the corresponding ‘ensemble’ and ‘single’ maps of Fig. 5.

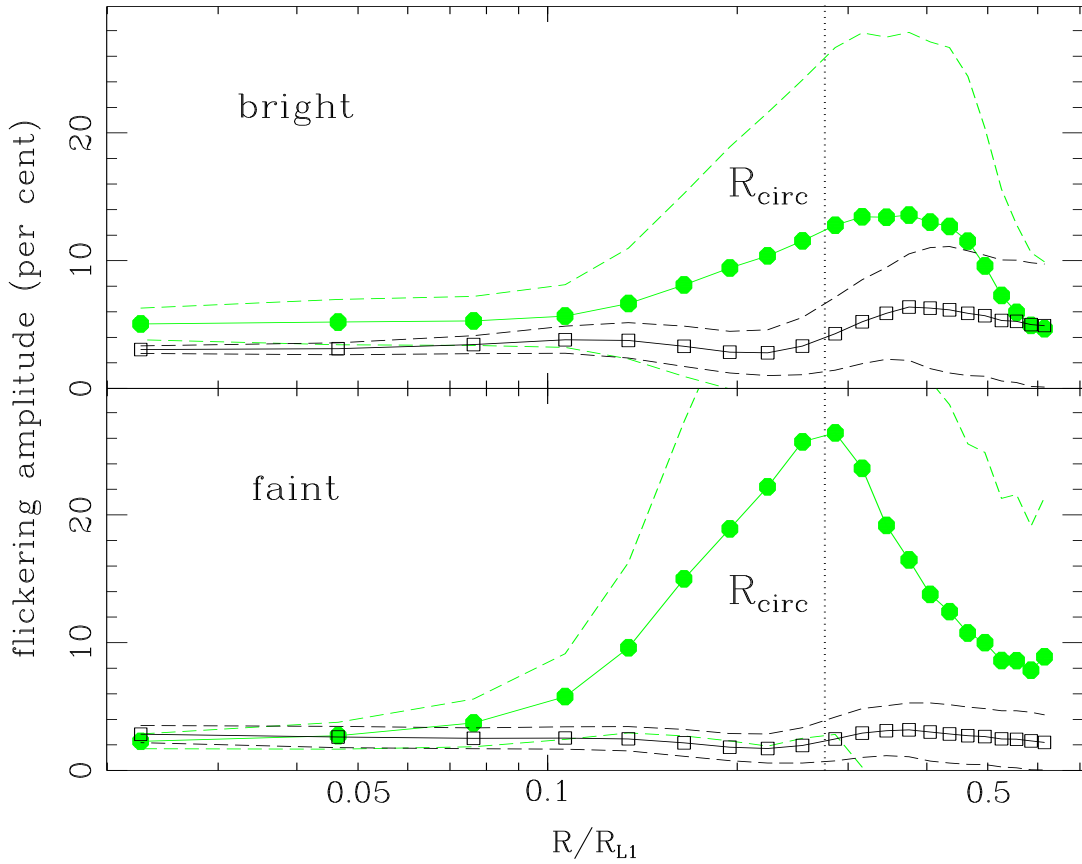


Fig. 8.— The relative amplitude of the flickering as a function of disk radius for the bright (top) and faint (bottom) states, from the 'ensemble' (filled circles) and 'single' (open squares) maps. The notation is the same as in Fig. 6.

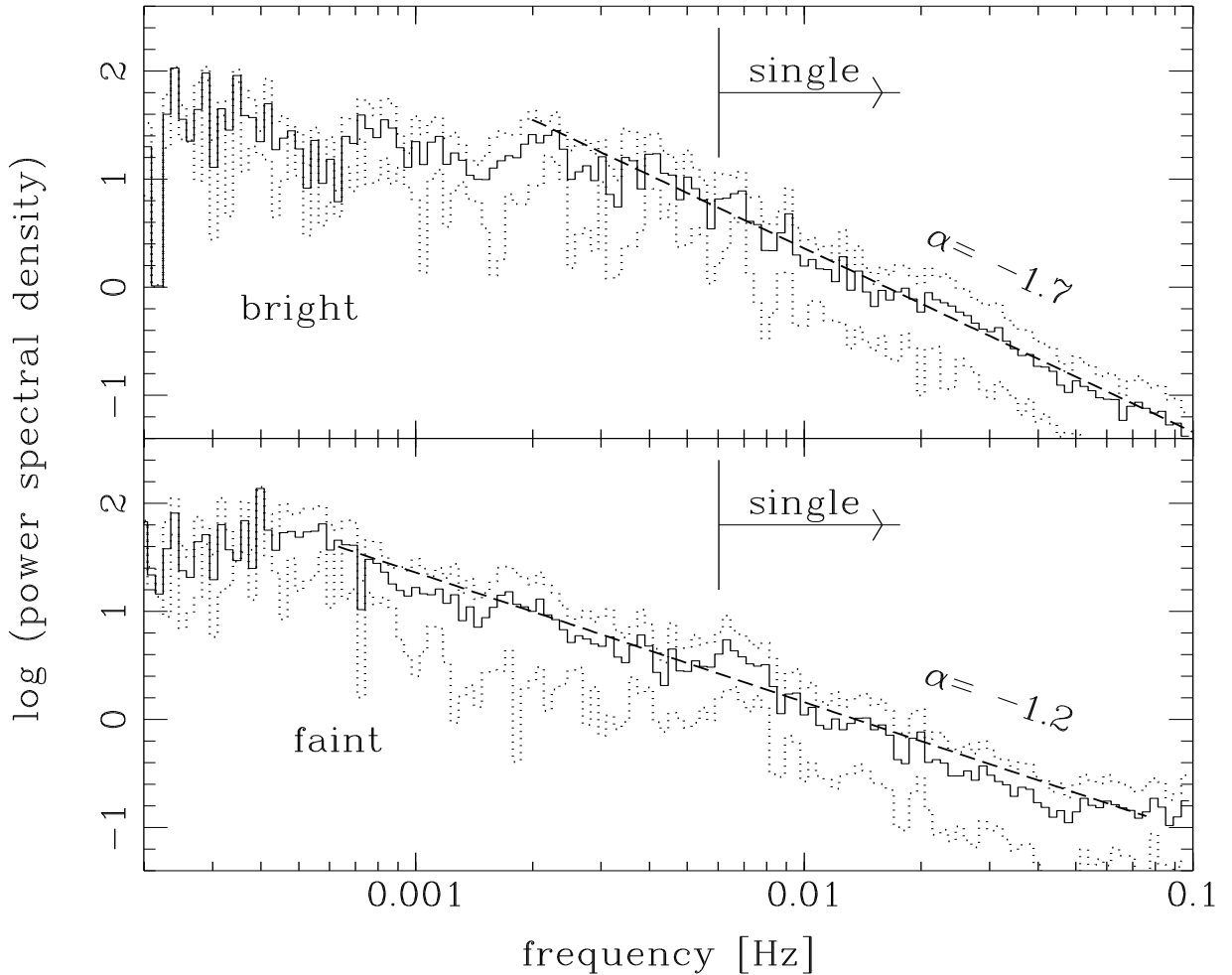


Fig. 9.— Average power spectrum density of the faint (bottom) and bright (top) states. The dotted lines show the $1-\sigma$ limits on the average power in each case. The best-fit power-law $P(f) \propto f^\alpha$ is shown as a dashed line in each panel and the corresponding slope is indicated. Vertical ticks mark the low-frequency cut-off of the filtering process applied to derive the ‘single’ scatter curves.

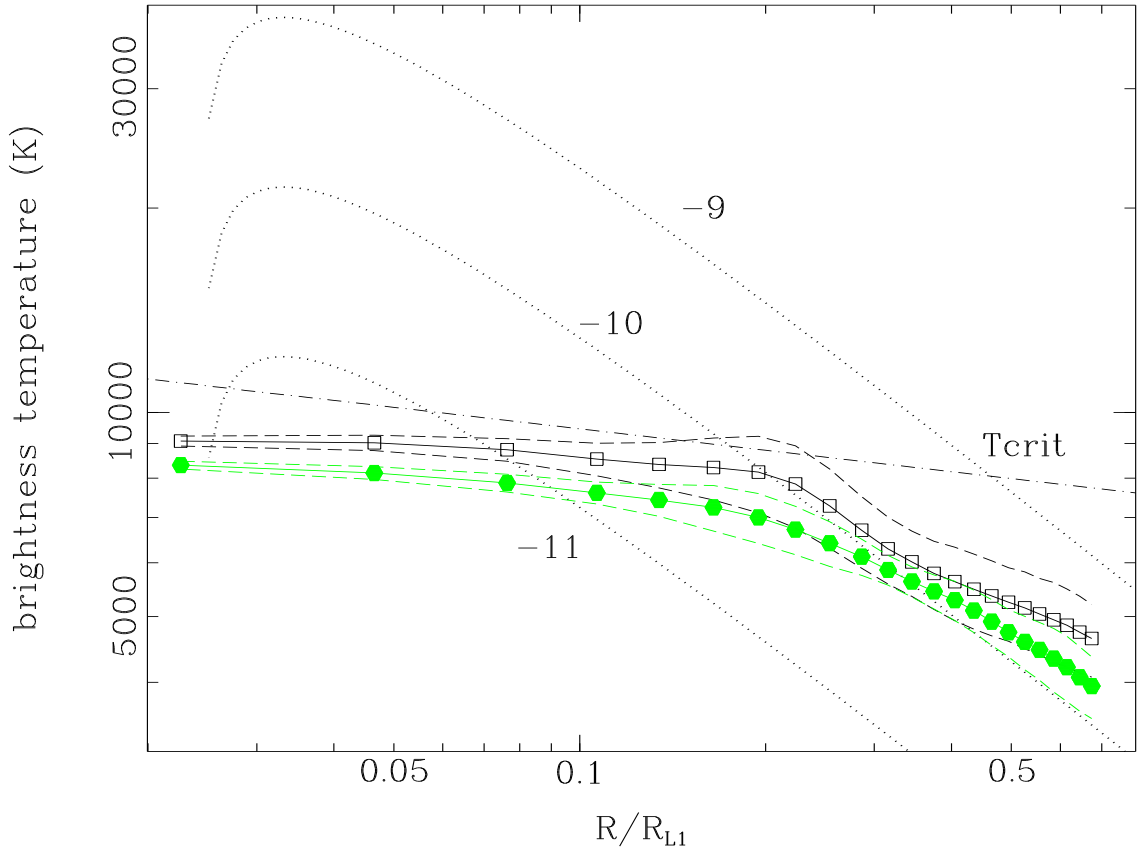


Fig. 10.— The brightness temperature radial distribution of the faint (filled circles) and bright (open squares) states, calculated assuming a distance of 146 pc to the system (Vrielmann et al. 2002) and no reddening. The dashed lines show the 1- σ limits on the average temperatures. Steady-state disk models for mass accretion rates of $\log \dot{M} = -9, -10, \text{ and } -11 M_{\odot} \text{ yr}^{-1}$ are plotted as dotted lines for comparison. These models assume $M_1 = 0.78 M_{\odot}$ and $R_1 = 0.0103 R_{\odot}$ (Baptista et al. 1998a). A dot-dashed line marks the critical temperature above which the gas should remain in a steady, high mass accretion regime according to the disc instability model (Warner 1995).

This figure "baptista.fig01.jpg" is available in "jpg" format from:

<http://arxiv.org/ps/astro-ph/0404261v1>

This figure "baptista.fig03.jpg" is available in "jpg" format from:

<http://arxiv.org/ps/astro-ph/0404261v1>

This figure "baptista.fig05.jpg" is available in "jpg" format from:

<http://arxiv.org/ps/astro-ph/0404261v1>